

Section 6

Developments in global forecast models, case studies, predictability investigations, global ensemble, monthly and seasonal forecasting

Ensemble assessment using the TIGGE database

Laurent Descamps, Carole Labadie, Alain Joly, Philippe Arbogast,
CNRM-GAME, Météo-France-CNRS, Toulouse

Ensemble forecasting has now become an important component of Numerical Weather Prediction. Several major meteorological centres have been running operational Ensemble Prediction Systems for years. Here, the purpose is to describe the Météo-France global ensemble forecasting system PEARP (Prévision d'Ensemble ARPEGE) designed for the short-range (from 72 to 108 h) probabilistic prediction and to present an evaluation of PEARP along with other ensembles using the TIGGE database (Bougeault et al., 2010).

The PEARP system

The operational version of PEARP is based on the ARPEGE model with an horizontal spectral truncation of T538 and a stretching factor of 2.4. The finer horizontal resolution is 15 km over France. There are 65 levels on the vertical up to a height of 50 km. The ensemble size is 35 members including a control member.

The initial perturbations of PEARP are built by combining the Météo-France ensemble data assimilation system AEARP (Berre et al., 2007) running at a coarser resolution (6 members, T399, no stretching) with singular vectors computed over different areas and with different optimization times and norms.

“Multi-physics” approach is used to represent model uncertainties. 10 different physical parametrization sets, including the ARPEGE operational physical package, have been chosen (Descamps et al, 2011).

Assessment of PEARP and other TIGGE ensembles

We present here an objective assessment of PEARP and four ensemble prediction systems: the UKMO ensemble prediction system (MOGREPS), the Canadian Meteorological Center (CMC) ensemble prediction system, the NCEP Global Ensemble Forecast System (GEFS) and the ECMWF ensemble prediction EPS. So far, most of the studies using the TIGGE database primarily have focused on medium-range prediction. The evaluation is here dedicated to short and early medium-range forecast.

Evaluation is provided for two synoptic variables, 500 hPa geopotential height, and 850 hPa temperature. Both variables are interpolated to a 1.5° latitude-longitude regular global grid using the interpolation routines provided by the TIGGE data portal (see the TIGGE portal at <http://tigge.ecmwf.int>) and run over a one-month period (September 2010).

A bootstrap resampling technique (Efron and Tibshirani (1993)) is applied to estimate confidence intervals (5%-95%) for the different scores. Our procedure is the same as the one used in Candille et al. (2007). We recompute the scores 10000 times with a sample of realizations randomly extracted, with replacement, from the original dataset.

A perfectly reliable ensemble and the observations are supposed to have the same climatology. In other words, the rank histogram, also known as the Talagrand diagram, is supposed to be flat. The delta score measures the departure from flatness. Fig 1 displays delta scores for the five global ensembles considered in this study. The results present common features in the sense that the reliability increases with lead-time for all the ensembles and for both variables considered here. For both variables CMC ensemble appears as the most reliable one, followed by PEARP except at very short ranges for the 500 hPa geopotential height.

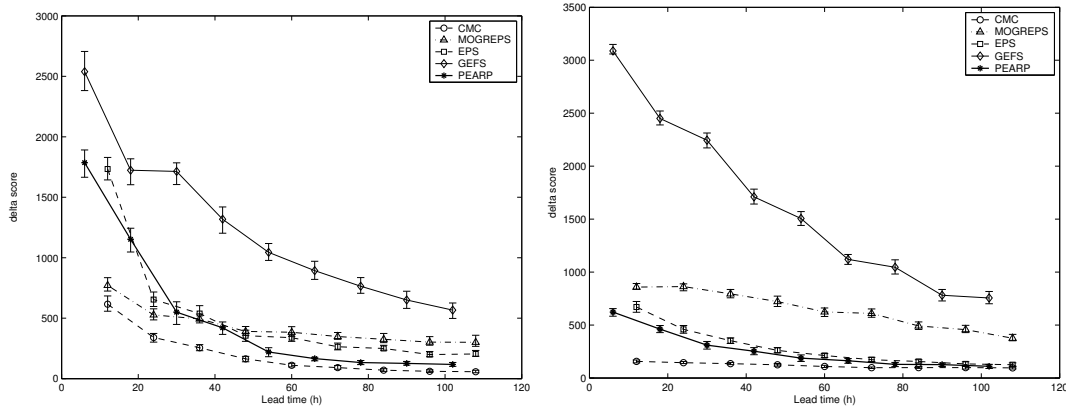


Figure 1: Global “delta” scores against radiosounding observations for a 1-month period for 500 hPa height (left) and 850 hPa temperature (right)

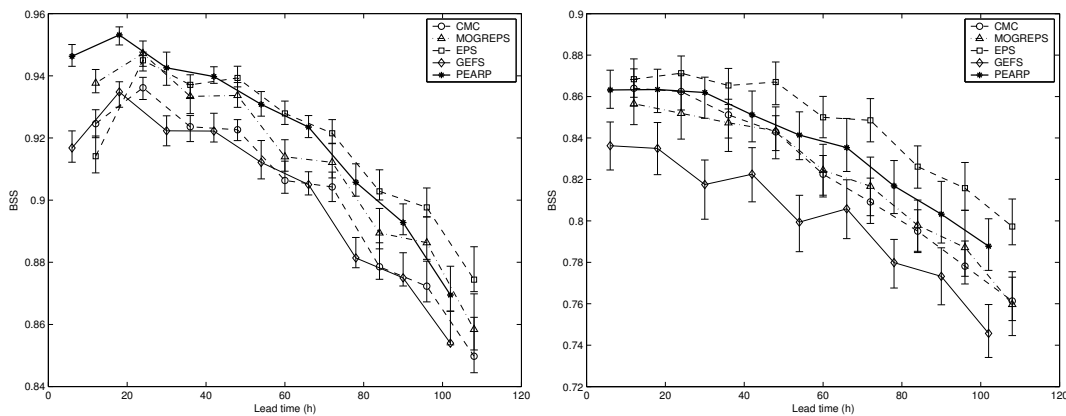


Figure 2: Global Brier Skill Scores scores against radiosounding observations for a 1-month period and for 500 hPa height (left) and 850 hPa temperature (right)

The Brier score measures a distance between the ensemble pdf and the observations. Although Brier score account for both the reliability and the resolution, it is dominated by the resolution term. A perfect ensemble has a Brier Skill Score (BSS) equal to 1. Fig 2 presents the BSS for the same ensembles and over the same period. Four among the five ensembles are very close with respect to the magnitude of the error bars. ECMWF ensemble seems to outperform the other ones except at very short ranges where PEARP behaves well.

References

- Berre, L., O. Pannekoucke, G. Desroziers, S. E. Stefanescu, B. Chapnik, and L. Raynaud, 2007: A variational assimilation ensemble and the spatial filtering of its error covariances: increase of sample size by local spatial averaging. ECMWF Workshop on Flow-dependent aspects of data assimilation, Reading, 151–168.
- Bougeault, P., et al., 2010: The Thorpex Interactive Grand Global Ensemble (TIGGE). Bull. Amer. Meteor. Soc., 91, 1059–1072.
- Candille, G., C. Côté, P. Houtekamer, and G. Pellerin, 2007: Verification of an ensemble prediction system against observations. Mon. Wea. Rev., 135, 2668–2699.
- Descamps, L., C. Labadie, and E. Bazile, 2011: Representing model uncertainty using the multiparametrization method. Proceedings of ECMWF Workshop on Model Uncertainty.
- Efron, B. and R. Tibshirani, 1993: An Introduction to the Bootstrap. Chapman & Hall, 436pp.

Operational Implementation of Modification to Stratocumulus Parameterization Scheme in JMA's Global Spectral Model

Takahiro Furukawa¹ and Akira Shimokobe^{1,2}

¹Numerical Prediction Division, Japan Meteorological Agency

²Department of Meteorology, School of Ocean and Earth Science and Technology,
University of Hawaii at Manoa

Email: furukawa@met.kishou.go.jp, akiras@hawaii.edu

Stratocumulus parameterization is implemented in the operational Global Spectral Model (GSM) of the Japan Meteorological Agency (JMA) to represent subtropical marine stratocumulus clouds off the western coast of continents. This parameterization is designed to work under the conditions of a strong inversion layer, and diagnoses the cloud fraction as a function of inversion strength. It normally has a positive effect that makes the radiation budget in regions of subtropical marine stratocumulus cloud more consistent with observed values (Kawai and Inoue, 2006). However, it eventually causes spurious clouds over dry regions (such as the Sahara and inland North America) and in dry conditions over the Sea of Japan because no information on water vapor is considered in the conditions under which the scheme is operated. Shimokobe (2012) showed that the addition of a new relative humidity threshold to the conditions reduces the incidence of spurious clouds and mitigates low-temperature bias in the lower troposphere with the low-resolution (TL319L60) global data assimilation and forecast system. In this study, the effects of the modification (in which a relative humidity threshold of more than 80% is added to the conditions) were investigated in a high-resolution (TL959L60) experiment. The threshold value of 80% was selected so that necessary subtropical marine stratocumulus clouds are maintained as much as possible and spurious clouds are eliminated as appropriate. Here, the previous model is referred to as CNTL, and the modified model is referred to as TEST.

Figure 1 shows cloud forecasts in CNTL and TEST around Japan. The spurious cloud by the stratocumulus scheme over the Sea of Japan seen in CNTL correctly disappears in TEST in comparison with visible image of MTSAT.

Figures 2 to 4 show the results obtained from global data assimilation and the forecast system with the same implementation as operational. Figure 2 indicates differences at a forecast time of 12 hours between TEST and CNTL averaged for August 2011 at 00 UTC. It can be seen that the frequency of stratocumulus scheme operation in TEST decreases in dry regions as intended. In addition, surface downwelling shortwave radiation grows and the temperature in the lower troposphere increases in areas where the stratocumulus scheme operation is suppressed. Figure 3 shows monthly average temperature differences at 850 hPa between radiosonde observations and the 12-hour forecast for August 2011 at 00 UTC. For CNTL, the model temperatures at 850 hPa are lower than the radiosonde observations at many stations. For TEST, however, the model temperatures are close to the observed values as per the differences seen in Figure 2.

Figure 4 shows the improvement ratio of TEST compared to CNTL in terms of the root mean square error (RMSE) of forecast values against analysis for forecasts covering periods from one to eleven days in August 2011 and January 2012. Significant positive impacts are seen on temperature at 850 hPa for all regions in forecast periods exceeding three-days forecast time during both periods. The RMSEs of other variables are also improved or neutral. These results are consistent with those of the low-resolution experiment conducted by Shimokobe (2012). This modified model has been in operation since December 18, 2012.

References

- Kawai, H. and T. Inoue, 2006: A simple parameterization scheme for subtropical marine stratocumulus. *SOLA*, **2**, 17 – 20.
- Shimokobe, A., 2012: Improvement of the Stratocumulus Parameterization Scheme in JMA's Operational Global Spectral Model. *CAS/JSC WGNE Research Activities in Atmospheric and Oceanic Modelling*, **42**, 4.17 – 4.18.

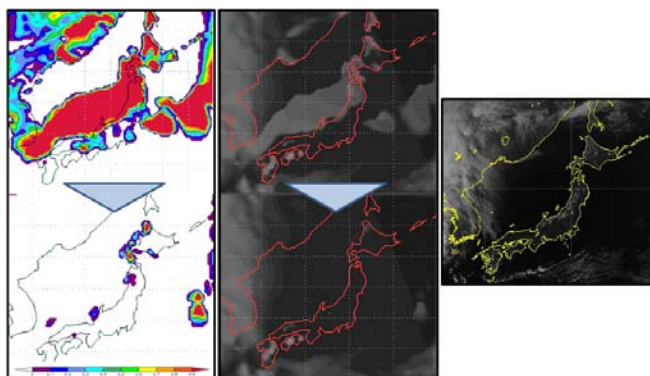


Figure 1: Cloud at a forecast time of 18 hours in TEST (top) and CNTL (bottom) around Japan on April 6, 2011 at 06 UTC. The panels on the left show the frequency of stratocumulus scheme operation in integration time steps from the previous six hours, those in the center show simulated visible cloud images of the GSM and that on the right shows MTSAT visible imagery.

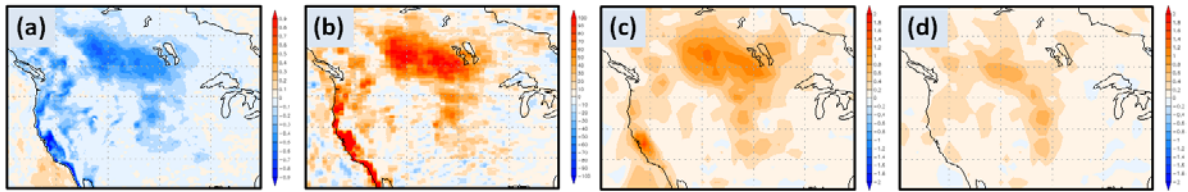


Figure 2: Differences between TEST and CNTL (TEST-CNTL) at a forecast time of 12 hours in North America for August 2011 at 00 UTC. (a) Frequency of stratocumulus scheme operation in integration time steps from the previous six hours, (b) surface downwelling shortwave radiation [W/m^2], (c) temperature [K] at 925 hPa, (d) temperature [K] at 850 hPa.

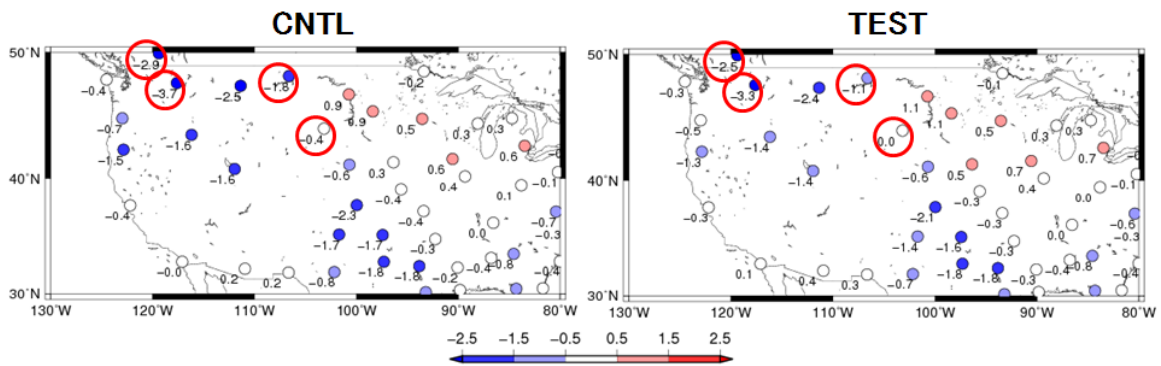


Figure 3: Monthly average bias of temperature [K] at 850 hPa against radiosonde observations for a forecast time of 12 hours in North America for August 2011 at 00 UTC. Observation stations with a bias difference between TEST and CNTL exceeding 0.4 K are circled in red.

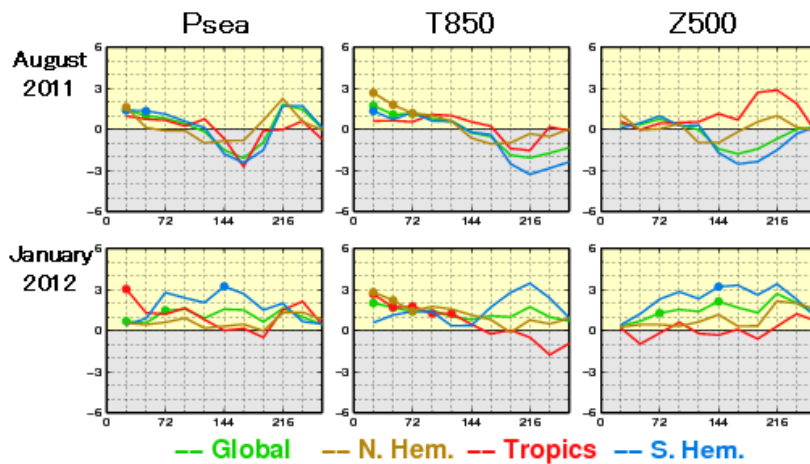


Figure 4: Improvement ratios (%) of TEST to CNTL in the RMSEs of forecasts against analysis for 1-11 day forecasts in August 2011 (top) and January 2012 (bottom). The horizontal axis represents the number of forecast hours. The graph labeled “Psea” shows surface pressure, “T850” shows temperature at 850 hPa and “Z500” shows 500 hPa geopotential heights. The green, brown, red and blue lines show the forecast improvement ratio for the global, Northern Hemisphere, tropical and Southern Hemisphere regions, respectively. Lines appearing in the upper (yellow) area indicate reduced RMSEs. The dots on the score lines represent statistical significance.

Verification of the Extreme Forecast Index in JMA's Operational One-month Ensemble Prediction System

Satoko Matsueda and Yuhei Takaya
Climate Prediction Division, Japan Meteorological Agency
(E-mail: matsueda@met.kishou.go.jp)

Introduction

The European Centre for Medium-Range Weather Forecasts (ECMWF) developed the Extreme Forecast Index (EFI; Lalaurette 2002; 2003) and a revised version (EFIR; Zsótér, 2006) with weighted tails of probability distribution. Both types are capable of indicating the potential scale of extreme weather events. EFI and EFIR values are applied in JMA's operational one-month ensemble prediction system (EPS) (Harada and Takaya 2012). This report describes 850-hPa temperature (T850) verification for both forecasts, which are expected to help users clarify the risks posed by extreme climate events.

Data and verification methods

EFI and EFIR values are calculated for JMA's one-month 25-member ensemble prediction, which is performed every Sunday, Monday, Wednesday and Thursday. JRA-25/JCDAS (Onogi et al. 2007) data are used for verification. Extreme climatic events are defined as occurring when analysis data exceeds the 90th climatological percentile or falls below the 10th percentile. These percentiles are estimated from the analysis of 1981 – 2010 data.

To investigate the skill of EFI and EFIR in detecting extreme climatic events, focus was placed on scatter plots for analysis anomalies and EFI or EFIR, and on hit rates and the number of false alarms. Reference was made to the verification method of Petroliağis and Pinson (2012).

Verification results

The results presented here are for seven-day-mean forecast fields initialized from 1 March, 2011, to 31 December, 2012. It is important to understand the relationship between predicted EFI (or EFIR) values and actual anomalies. Figure 1 shows scatter plots for T850 analysis anomalies and

EFI/EFIR values for Kobe, Japan (35°N, 135°E) with lead times of 5 – 11 days. The greater index amplitudes corresponding to larger analysis anomalies suggest that EFI and EFIR are useful in predicting extreme climatic events. However, the values of these indices do not always relate to large analysis anomalies (e.g., when the EFI and EFIR figures are –0.6, analysis anomalies could be in the range from –6 to 0 K). Forecast errors also result in a wide range of EFI and EFIR values. The amplitude of EFIR is often larger than that of EFI because the former is highly sensitive to the tails of forecast probability distribution as reported by Zsótér (2006).

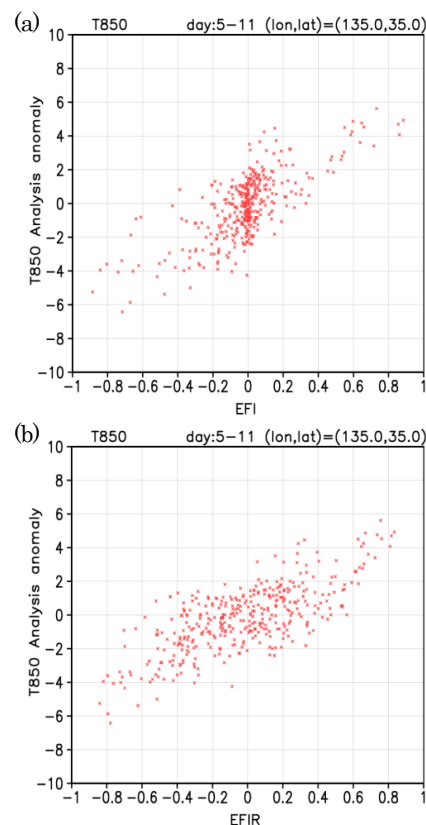


Figure 1 Scatter plots of (a) EFI and (b) EFIR values and analysis anomalies for T850 in Kobe, Japan (35°N, 135°E) with lead times of 5 – 11 days.

Figure 2 shows hit rates and the number of false alarms with EFIR for T850 extreme climatic events in Kobe. For example, the hit rate and false alarm rate for extremely high T850 values defined with an EFIR threshold of 0.6 are approximately 0.33 and 0.22, respectively. The hit rates for extremely low T850 values are higher than those for extremely high values, but the false alarm rates are also higher. These scores vary considerably depending on areas, lead times and forecast variables (not shown).

Summary

The results of verification for the EFI and EFIR judgments used in JMA's one-month EPS are expected to help users understand levels of forecast skill depending on areas, lead times and forecast variables. The risk of extreme climatic events can be determined based on the selection of an appropriate

EFI/EFIR threshold, and more detailed information can be obtained from other EPS products (e.g., EPS meteogram (Harada and Takaya 2012)).

References

- Lalurette, F., 2002: Early detection of abnormal weather conditions using a probabilistic extreme forecast index. *ECMWF Tech. Memorandum*, **373**.
- Lalurette, F., 2003: Early detection of abnormal weather conditions using a probabilistic extreme forecast index. *Quart. J. Roy. Meteor. Soc.*, **129**, 3037 – 3057.
- Onogi, K., J. Tsutsui, H. Koide, M. Sakamoto, S. Kobayashi, H. Hatsushika, T. Matsumoto, N. Yamazaki, H. Kamahori, K. Takahashi, S. Kadokura, K. Wada, K. Kato, R. Oyama, T. Ose, N. Mannoji and R. Taira, 2007: The JRA-25 Reanalysis. *J. Meteorol. Soc. Japan*, **85**, 369 – 432.
- Petroligis, T. I. and P. Pinson, 2012: Early indication of extreme winds utilising the extreme forecast index. *ECMWF Newsletter*, **132**, 13 – 19.
- Zsótér, E., 2006: Recent developments in extreme weather forecasting. *ECMWF Newsletter*, **107**, 8 – 17.

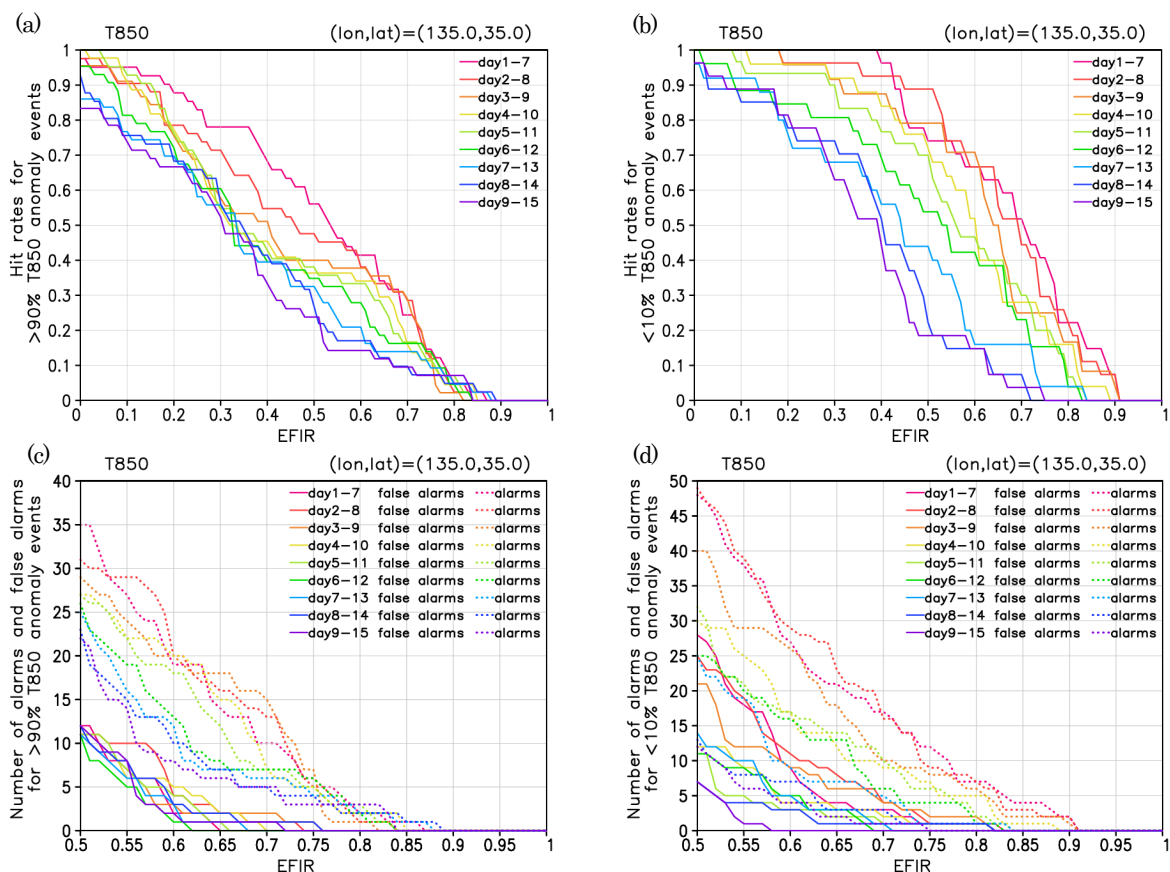


Figure 2 (a), (b) Hit rates and (c), (d) numbers of false alarms (solid lines) and valid alarms (dotted lines) based on different EFIR thresholds for T850 extreme events in Kobe, Japan (35°N, 135°E) defined with the thresholds of (a), (c) > 90th percentile and (b), (d) < 10th percentile. The line colors indicate different forecast lead times.

El Niño-Southern Oscillation Feedback in JMA's Seasonal Forecast Model

Satoko Matsueda and Yuhei Takaya
Climate Prediction Division, Japan Meteorological Agency
(E-mail: matsueda@met.kishou.go.jp)

Introduction

It is important for seasonal prediction to represent El Niño-Southern Oscillation (ENSO) appropriately in an atmosphere-ocean coupled global circulation model (CGCM). ENSO forecast skill in JMA's operational seasonal forecast model (JMA/MRI-CGCM) is comparable to that of models used in other major centers. However, the amplitude, frequency and spatial pattern of ENSO as predicted by the JMA model differ from the results of actual ENSO analysis. ENSO representation among CGCMs is diverse, and it has been suggested that atmospheric models play a dominant role in determining ENSO amplitude and frequency in CGCMs (Guilyardi et al. 2009). In this study, two types of atmospheric feedback (ENSO feedback) were diagnosed with reference to the method proposed by Lloyd et al. (2009).

Data

Single-member forecasts in a set of hindcasts were analyzed using JMA's CGCM with (CGCM_FLAD) and without flux adjustment (CGCM_NFLAD). Forecasts were initialized twice a month for CGCM_FLAD and once a month for CGCM_NFLAD for the period 1979 – 2008. An AMIP-type run with JMA's CGCM was also used for the period 1979 – 2010, a quasi-coupled data assimilation system data set (MOVE-C; Fujii et al. 2009) was used for the period 1979 – 2009, and JRA-55 reanalysis data (Ebita et al. 2011) were used for the period 1980 – 1999. The monthly mean fields of all variables were analyzed.

Diagnosis method for ENSO feedback

Lloyd et al. (2009) diagnosed two types of atmospheric feedback (dynamical and total heat flux) that have a dominant influence on ENSO. Dynamical feedback is represented as follows:

$$\tau_x' = \mu T'$$

This is known as Bjerknes feedback (Bjerknes 1969) –

a positive type in which a positive (negative) sea surface temperature (SST) anomaly (T') induces a westerly (easterly) wind stress anomaly (τ_x'), enhancing a positive (negative) SST anomaly.

The total heat flux feedback is represented as follows:

$$Q' = \alpha T'$$

This is considered to be a negative type in which a positive (negative) SST anomaly (T') increases (reduces) the total heat flux (Q), resulting in SST anomaly decay. Total heat flux feedback (α) consists of contributions from latent heat flux (LH), sensible heat flux (SH), short-wave radiative flux (SW) and long-wave radiative flux (LW).

Remote dynamical feedback μ , local dynamical feedback μ_L and local heat flux feedback α were calculated with reference to the method proposed by Lloyd et al. (2009). Results averaged for 1 – 7 forecast months were shown as CGCM diagnostics.

Diagnosis results

Figure 1 shows ENSO feedback estimated from each type of data. The dynamical (μ and μ_L) and total heat (α) feedback in CGCMs has the same sign as JRA-55 reanalysis results and is reasonable compared to that of CMIP3 models (Lloyd et al. 2009). However, the feedback is underestimated in CGCMs compared to JRA-55. For the AMIP run, μ and α are closer to JRA-55. Similar results were obtained from CMIP3 models (Lloyd et al. 2009 and Lloyd et al. 2011). MOVE-C also underestimates μ and α . Lloyd et al. (2009) suggested that α is related to ENSO amplitude and influences ENSO representation in coupled models. Figure 2 shows the values of four heat/radiative flux feedback components (α_{LH} , α_{SW} , α_{LW} , and α_{SH}). For all data, α_{LH} and α_{SW} are dominant, and α_{LH} is well represented. However the value of α_{SW} depends on the models, and can be seen as a significant factor contributing to errors in α

(Lloyd 2009). The amplitude of α_{SW} for the AMIP run is larger than that for CGCMs and similar to that for JRA-55. These characteristics are also seen with CMIP3 models (Lloyd et al. 2011). The spatial distribution of α_{SW} is shown in Figure 3. Negative feedback of α_{SW} in the NINO.3 region related to large-scale convective activity is reproduced by all models but is underestimated by CGCMs and MOVE-C compared to the results of JRA-55 and the AMIP run. Positive feedback of α_{SW} off the coast of Peru (in a region of large-scale subsidence) is overestimated by CGCMs compared to the results of JRA-55, and by most CMIP3 models (Lloyd et al. 2012). The underestimation of precipitation anomalies during ENSO events and poor representation of clouds over the tropics in models can be considered as possible reasons for this. The diagnostics presented here offer a way to clarify and assess the representation of ENSO feedback in atmospheric models.

References

- Ebita, A., S. Kobayashi, Y. Ota, M. Moriya, R. Kumabe, K. Onogi, Y. Harada, S. Yasui, K. Miyaoka, K. Takahashi, H. Kamahori, C. Kobayashi, H. Endo, M. Soma, Y. Oikawa and T. Ishimizu, 2011: The Japanese 55-year Reanalysis "JRA-55": An Interim Report. *SOLA*, **7**, 149 – 152.
- Fujii, Y., T. Nakaegawa, S. Matsumoto, T. Yasuda, G. Yamanaka and M. Kamachi, 2009: Coupled climate simulation by constraining ocean fields in a coupled model with ocean data. *J. Climate*, **22**, 5541 – 5557.
- Guilyardi, E. et al., 2009: Understanding El Niño in ocean-atmosphere general circulation models: Progress and challenges. *Bull. Amer. Meteor. Soc.*, **90**, 325 – 340.
- Lloyd, J., E. Guilyardi, H. Weller and J. Slingo, 2009: The role of atmosphere feedbacks during ENSO in the CMIP3 models. *Atmos. Sci. Lett.*, **10**, 170 – 176.
- Lloyd, J., E. Guilyardi, H. Weller, and J. Slingo, 2011: The role of atmosphere feedbacks during ENSO in the CMIP3 models. Part II: Using AMIP runs to understand the heat flux feedback mechanisms. *Climate Dyn.*, **37**, 1271 – 1292.
- Lloyd, J., E. Guilyardi, H. Weller, 2012: The role of atmosphere feedbacks during ENSO in the CMIP3 Models. Part III: the shortwave flux feedback. *J. Climate*, **25**, 4275 – 4293.

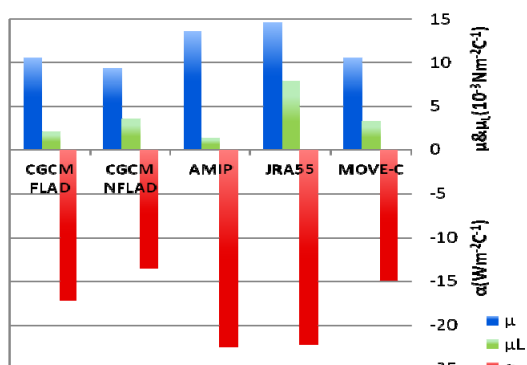


Figure 1 Average annual NINO.4 μ (blue), NINO.3 μ (green) and NINO.4 α (red) values for CGCM_FLAD, CGCM_NFLAD, AMIP run, JRA-55 and MOVE-C

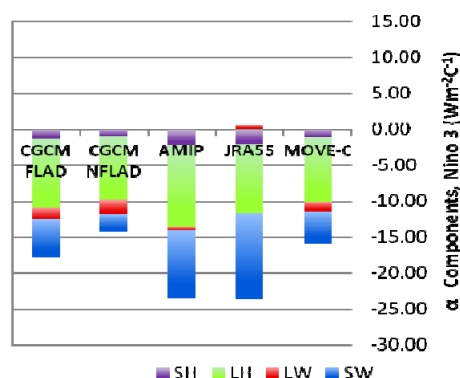


Figure 2 Average annual α components: α_{SH} (purple), α_{LH} (green), α_{LW} (red) and α_{SW} (blue) for CGCM_FLAD, CGCM_NFLAD, AMIP run, JRA-55 and MOVE-C

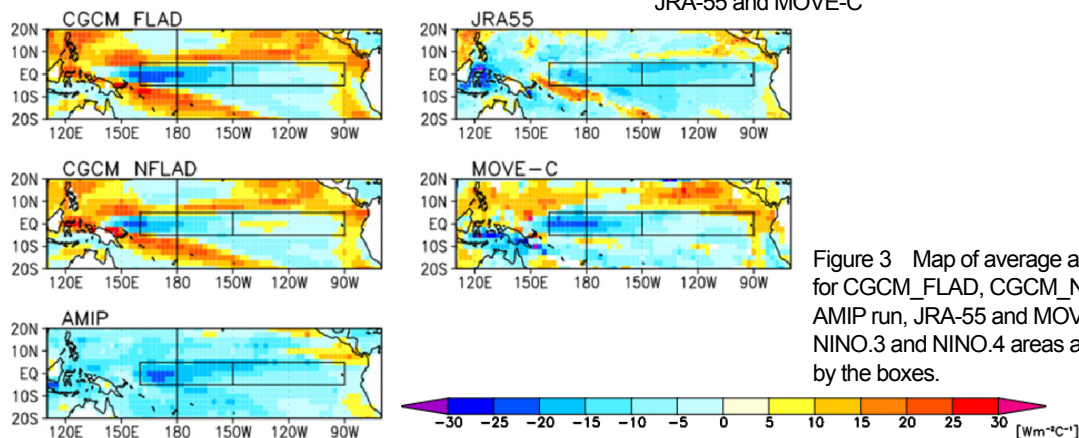


Figure 3 Map of average annual α_{SW} , for CGCM_FLAD, CGCM_NFLAD, AMIP run, JRA-55 and MOVE-C. The NINO.3 and NINO.4 areas are shown by the boxes.

The Navy Global Environmental Model

T. Hogan (Timothy.Hogan@nrlmry.navy.mil), M. Peng, N. Baker, C. Reynolds, B. Ruston, M. Liu, J. Ridout, S. Eckermann¹, J. Moskaitis, T. Whitcomb, K. Viner, J. McLay, P. Pauley, L. Xu, R. Langland, M. Flatau, J. McCormick¹, and S. Chang

Marine Meteorology Division, Naval Research Laboratory, Monterey, CA, USA

¹Space Science Division, Naval Research Laboratory, Washington, DC, USA

The Navy Global Environmental Model (NAVGEN) is the U.S. Navy's new high-resolution global weather prediction system, replacing the existing Navy Operational Global Atmospheric Prediction System (NOGAPS) which was introduced in 1982. Development of NAVGEN was sponsored by ONR and OPNAV N2/N6E (Oceanographer of the Navy). NAVGEN represents a significant NRL milestone in Numerical Weather Prediction (NWP) system development by introducing a Semi-Lagrangian/Semi-Implicit (SL/SI) dynamical core together with advanced moisture and ozone physical parameterization schemes. The new SL/SI dynamic core allows for much higher model resolutions without the need for small time steps. This capability has permitted NAVGEN's initial operational transition to have both higher horizontal and vertical resolutions than NOGAPS (50 vertical levels in place of NOGAPS's 42 levels and an increase of horizontal resolution from 42 km to 37 km) and also to include cloud liquid water, cloud ice water, and ozone as fully predicted constituents, contain new moisture, solar radiation and longwave-radiation parameterizations, and significant upgrades to the data assimilation component and to complete the 180-hour forecast in the allotted operation window.

Critical to NAVGEN's success is the new SL/SI dynamical core. The SL method is to find the trajectory of the fluid motion that starts at the previous time step and ends up at the NAVGEN grid point location.¹ The SL integration removes the Courant-Friedrichs-Lewy (CFL) limitation of NOGAPS for conventional fixed point integration of the dynamical equations, however high-speed gravity waves associated with high-frequency fluctuations in the wind divergence, remain. This is mitigated by incorporating a SI method into the SL integration, where the terms responsible for the gravity waves are identified and treated in an implicit manner, thereby slowing down the fastest gravity waves. The combined SL/SI schemes have enabled NAVGEN to run with a time step that is three times faster than NOGAPS.

With the addition of cloud liquid water and cloud ice water advection, NRL has developed a new 2-species micro-physics cloud water parameterization based on the work of Zhao.² Convective clouds are allowed to evaporate at a finite rate that varies with cloud cover, providing for a more realistic representation of convective processes. This feature is enhanced by detraining cloud condensate between the lifting condensation level and the level of free convection in the NAVGEN modified versions of the Simplified Arakawa Schubert and the National Centers for Environmental Prediction's (NCEP) Global Forecast System's (GFS) shallow convection schemes.

Another significant improvement in NAVGEN is the addition of the Rapid Radiative Transfer Model for General Circulation Models (RRTMG) parameterizations for solar and longwave radiation, developed by the Atmospheric Environment Research Inc.³ RRTMG includes significantly more radiation frequency bands in the solar and longwave spectra than the previous NOGAPS radiation parameterizations and incorporates additional molecular absorbers and emitters. A unique feature of the RRTMG is the use of a Monte-Carlo technique to compute the sub-grid cloud variability and the vertical cloud overlap.

Satellite radiance observations typically account for more than 65% of the total assimilated observations in NAVGEM. The data assimilation component that brings these observations into NAVGEM is the NRL Atmospheric Variational Data Assimilation System – Accelerated Representer (NAVDAS-AR), which has been operational in NOGAPS since 2009.⁴ The NOGAPS radiance bias correction method has been replaced in NAVGEM with a variational bias correction approach, which estimates the bias predictors simultaneously with the atmospheric analysis during each data assimilation cycle.⁵ This way, the bias corrections are constrained by other observations, the NWP model, and the analysis procedure itself.

Verification of NAVGEM's accuracy shows significant improvements over NOGAPS. The Northern Hemisphere 1000 hPa geopotential height anomaly correlations (AC) for summer 2012 and fall/winter 2012-13 shows a 6 hour improvement over the NOGAPS forecasts at 120 h. Tropical cyclone (TC) track forecasts are of vital importance to the safety of U.S. Navy ships, aircraft, and personnel. TC track error comparisons for summer/fall 2012 indicate that the NAVGEM 120-h TC track error is 30 nautical miles less than NOGAPS, approximately a 12-hour improvement. Synoptic evaluations of daily weather maps show reduced surface pressure errors with NAVGEM, particularly for maritime lows that impact the safety of ships at sea. In addition, the mid-level troughs associated with frontal systems were more realistic (deeper and faster moving) in NAVGEM than in NOGAPS.

An official operational test (OPTTEST) of NAVGEM versus NOGAPS was conducted by Fleet Numerical Meteorology and Oceanography Center (FNMOC) for the period of 6 November 2012 – 18 December 2012 with a statistical evaluation based on FNMOC's standard global scorecard. This scorecard evaluates the comparative skill of the models based on AC, mean and root mean square errors of 16 different fields and observation types, including TC tracks, 10-meter winds at buoy sites, 1000 hPa and 500 hPa AC, and winds and temperatures at radiosonde locations, assigning a weighted positive score to the model with statistically-significant better forecasts. Improvements in all categories would yield a skill score of +24. NAVGEM scored a +14, the highest score ever obtained for a global model transition at FNMOC. Historically, global model improvements resulted in a skill improvement of +2. NRL will continue to upgrade NAVGEM with planned transitions to higher vertical and horizontal resolutions, a more computationally efficient dynamical core, further improvements to the data assimilation system, more advanced physical parameterizations, and the assimilation of data from recently-launched satellite sensors.

References:

¹Ritchie, H. 1991: Application of the semi-Lagrangian method to a multilevel spectral primitive equation model. *Q. J. R. Meteorol. Soc.*, **117**, 91-106.

²Zhao, Q. Y., and F. H. Carr, 1997: A prognostic cloud scheme for operational NWP models. *Mon. Wea. Rev.*, **125**, 1931-1953.

³Pincus, R., H.W. Barker, and J.-J. Morcrette, 2003: A fast, flexible, approximate technique for computing radiative transfer in inhomogeneous clouds. *J. Geophys. Res.*, **108(D)**, 4376.

⁴Chua, B., L. Xu, T. Rosmond, and E. Zaron, 2009: Preconditioning representer-based variational data assimilation systems: application to NAVDAS-AR. *Data Assimilation for Atmospheric, Oceanic and Hydrologic Applications*, Springer-Verlag, 493 pp.

⁵Dee, D., 2004: Variational bias correction of radiance data in the ECMWF system. Pp. 97-112 in Proceedings of the ECMWF workshop on assimilation of high spectral resolution sounders in NWP, 28 June-1 July 2004, Reading, UK.

A Method of Predicting Sea Ice Boundary Conditions for the One-month Ensemble Prediction System

Hiroyuki Sugimoto and Yuhei Takaya
Climate Prediction Division, Japan Meteorological Agency, Tokyo, Japan
(E-mail: h-sugimoto @ met.kishou.go.jp)

1. Introduction

A method of predicting daily sea ice distribution was developed to determine sea ice boundary conditions for JMA's one-month ensemble prediction system (EPS), which employs an atmospheric global circulation model (AGCM). Sea ice distribution for the coming month is predicted based on initial sea ice concentration (SIC) anomalies in ocean grids and initial sea ice extent (SIE) anomalies in the Northern and Southern Hemispheres with reference to the method proposed by Mizuta et al. (2008). The skill of these sea ice distribution predictions is better than that of the climatological distributions used in JMA's current operational one-month EPS.

2. Data and sea ice area definition

The SIC used to predict sea ice distribution comes from satellite-based daily data sets covering the period from 1986 to 2010 as analyzed by JMA (Ishii et al. 2005), and the horizontal resolution is 0.25 degrees.

Ocean grids with SIC values exceeding 55% are defined as sea ice areas and others are defined as open sea based on the SIC threshold of sea ice grids in the AGCM. The climatological sea ice presence frequency for each grid is determined from 31-day running means of daily presence frequency for the period between 1986 and 2010.

3. Procedure for daily sea ice prediction

Daily sea ice distribution is predicted using a combination of persistent initial SIC anomalies observed in ocean grids and persistent initial SIE anomalies in the Northern and Southern Hemispheres. The procedure for such prediction is described below and presented as a diagram in Fig. 1.

Initial date

Initial sea ice distribution is determined by identifying ocean grids as either sea ice or open-sea types based on the SIC threshold (55%). Initial SIC anomalies in ocean grids and initial SIE anomalies in the Northern and Southern Hemispheres are also calculated.

Lead times of less than 14 days

With lead times of less than 14 days, SICs predicted for ocean grids are assumed to be persistent initial

anomalies, which requires the addition of initial SIC anomalies to daily climatological SICs. Ocean grids are identified as either potential sea ice or potential open-sea types based on the SIC threshold (55%). Sea ice distribution is then predicted by adjusting the potential distribution so that the initial SIE anomalies in each hemisphere persist, which means that potential sea ice (open-sea) grids with lower (higher) climatological frequency are modified to open-sea (sea ice) grids.

Lead times of more than 15 days

With lead times of more than 15 days, sea ice distribution is predicted by adjusting the previous day's distribution so that initial SIE anomalies in each hemisphere persist. In other words, the predicted SIE anomaly is made equal to the initial anomaly by correcting sea ice and open-sea grids based on climatological presence frequencies. During the sea ice development (melting) season, previous open-sea (sea ice) grids with higher (lower) frequencies are converted to sea ice (open-sea) grids.

4. Verification

Equitable threat scores were used to verify the accuracy of sea ice distribution predictions. Figure 2 shows such verification based on four methods involving the use of persistent initial SIC anomalies, persistent initial SIE anomalies, a combination of both, and sea ice climatologies. The combined method is the most skillful except for January due to sparse Antarctic sea ice distribution, which exacerbated the scale of estimation errors.

5. Summary and future plans

In this work, a method of predicting sea ice boundary conditions for JMA's one-month EPS was developed. The approach was found to provide sea ice distribution values that correspond to the results of actual analysis. Daily sea ice distributions predicted using this method are to be introduced in the next update of JMA's one-month EPS. Arctic sea ice retreat related to global warming (IPCC 2007) is also expected to be taken into account, and the skill of one-month EPS prediction is expected to improve.

References

- IPCC, 2007: Climate Change 2007: The Physical Science Basis. Contribution of Working Group I to the Fourth Assessment Report of the Intergovernmental Panel on Climate Change [Solomon, S., D. Qin, M. Manning, Z. Chen, M. Marquis, K. B. Averyt, M. Tignor and H. L. Miller (eds.)]. Cambridge University Press, Cambridge, United Kingdom and New York, NY, USA, 996pp.
- Ishii, M., A. Shouji, S. Sugimoto and T. Matsumoto, 2005: Objective analyses of sea-surface temperature and marine meteorological variables for the 20th Century using ICOADS and the Kobe Collection. *Int. J. Climatol.*, **25**, 865-879.
- Mizuta, R., Y. Adachi, S. Yukimoto and S. Kusunoki, 2008: Estimation of the Future Distribution of Sea Surface Temperature and Sea Ice Using the CMIP3 Multi-model Ensemble Mean. *Technical Reports of the Meteorological Research Institute*, **56**, 28pp.

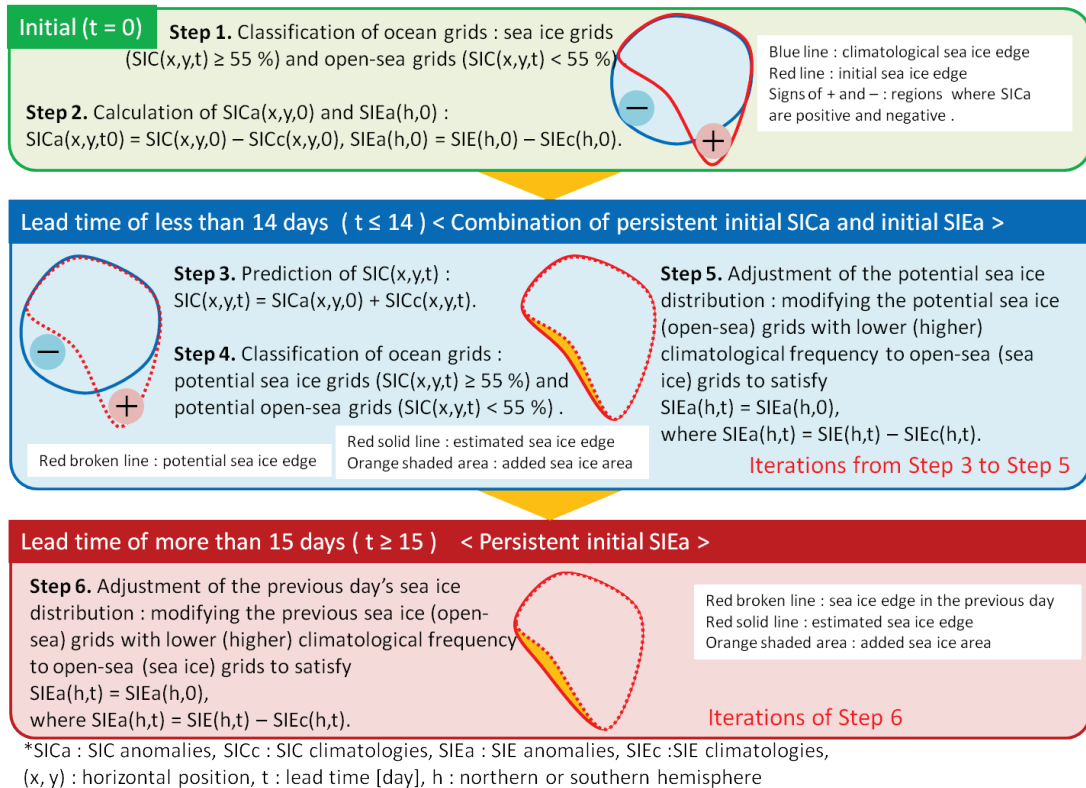


Fig. 1 Summary of sea ice prediction method

In Step 5, the potential SIE anomaly is smaller than the initial anomaly. Step 6 is for the sea ice development season.

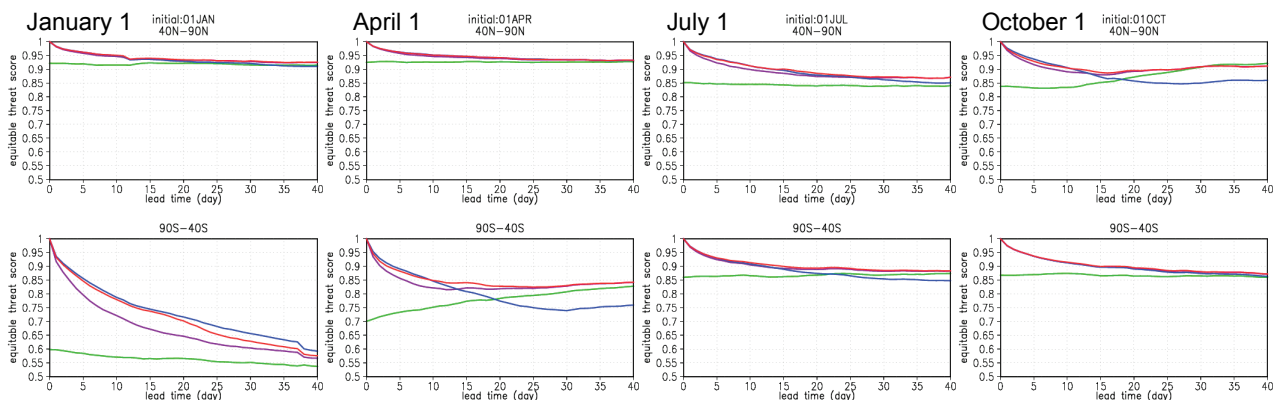


Fig. 2 Equitable threat scores for sea ice distribution predicted using four methods

The x-axis shows the lead time from the initial date, and the y-axis shows the equitable threat score. Scores are calculated for the period from 1986 to 2010, and the initial dates (from left to right) are January 1, April 1, July 1 and October 1. The upper figures are for the Arctic and the lower ones are for the Antarctic. The red, blue, purple and green lines show scores based on the proposed method, persistent initial SIC anomalies, persistent initial SIE anomalies and climatological distributions, respectively.